SrSnO$_3$ Perovskite post-deposition on Ag-doped TiO$_2$ rutile nanoflower for optoelectronic application

Nurul Najihah Ishak [a], Nafarizal Nayan [b], Megat Muhammad Ikhsan Megat Hasnan [c], Noor Kamalia Abd Hamed [b], Yusri Md Yunos [a], Mohamed Sultan Mohamed Ali [a,*]

[a] Faculty of Electrical Engineering, Universiti Teknologi Malaysia, 81310, UTM Johor Bahru, Johor, Malaysia
[b] Microelectronics & Nanotechnology-Shamsuddin Research Centre (MiNT-SRC), Universiti Tun Hussein Onn Malaysia, 86400, Batu Pahat, Johor, Malaysia
[c] Faculty Engineering Electric and Electronic, Universiti Malaysia Sabah, 88400, Kota Kinabalu, Sabah, Malaysia

HIGHLIGHTS

- Incorporating SrSnO3 in Ag-doped Rutile TiO2 Nano Flower boosts photo-anode surface area.
- Ag-doped rT-NF/SrSnO3 with varying Ag dopant shows optical bandgap shift.
- Ag-doped rT-NF/SrSnO3 creates rough surface for effective light scattering.
- SrSnO3 in Ag-doped rT-NF enhances electron mobility, suppresses charge recombination.
- Ag-doped rT-NF/SrSnO3 exhibits remarkable photoresponse under visible spectrum.

GRAPHICAL ABSTRACT
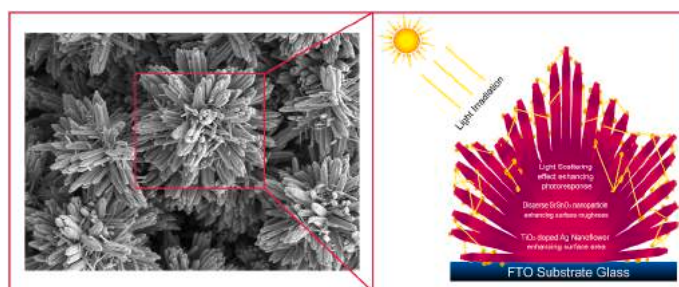
ARTICLE INFO

ABSTRACT

Optoelectronic nanomaterials could be improved through bandgap engineering and surface area enhancement, which involves depositing nanoparticles on their photoactive layer surfaces. The present study investigated silver-doped rutile nanoflower TiO$_2$ with an additional surface layer of perovskite SrSnO$_3$ nanoparticles (rT-NF) using a combination of hydrothermal pre-processing followed by radio frequency (RF) magnetron sputtering. The new structure exhibited expanded visible spectrum light absorption. Increasing SrSnO$_3$ deposition time lowered the energy bandgap from 3.0 eV to 2.89 eV. Furthermore, the electrical impedance approach and current-voltage measurement revealed the material's electrical properties, subsequently supported by structural and surface characterization via XRD, FESEM, AFM, and Raman Spectroscopy. The post-deposition of SrSnO$_3$ perovskite on Ag-doped rT-NF raised rutile crystallinity, enhanced its photo response, and lowered its bandgap and bulk resistivity. The outcomes of this work provided a new route to enhancing standard TiO$_2$ nanoflower photoelectric response via perovskite post-deposition on nanoflower surfaces.

1. Introduction

Solar cells used for electricity generation are one application of optoelectronics. Dye-sensitized solar cells (DSSC) are a novel variant consisting of a semiconductor photoanode, dye-sensitizer, electrolyte, and counter electrode. During the lighting stage, photons in the dye
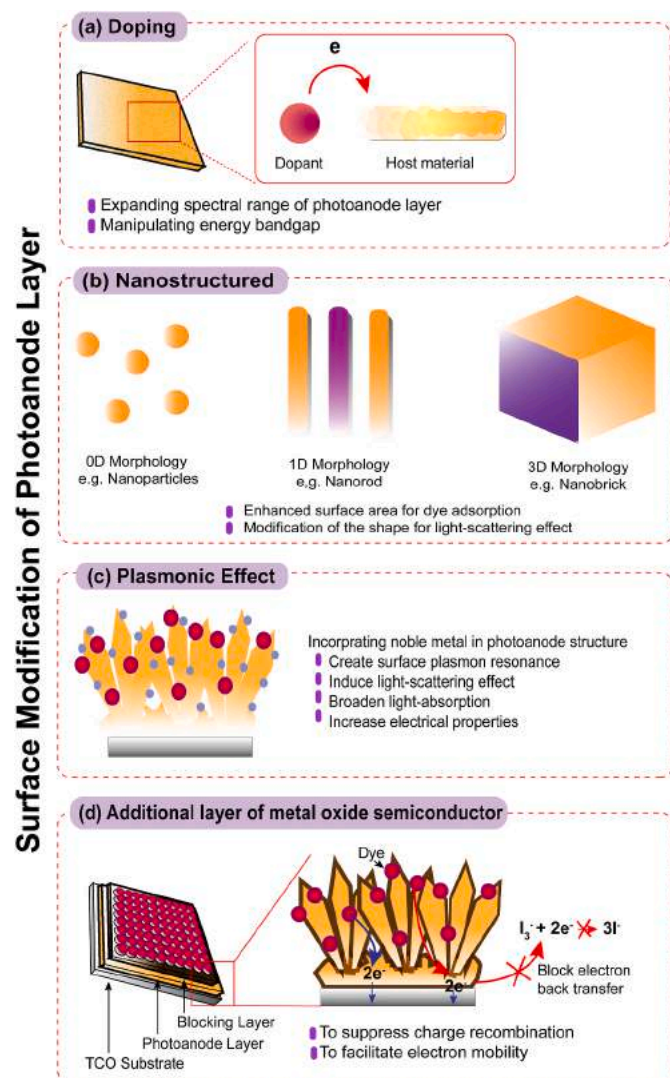

Fig. 1. Surface modification of photoanode layer. (a) Incorporating ion-doping in photoanode structure for optical properties enhancement. (b) Tailoring nanostructured morphology for light-scattering enhancement. (c) Create plasmonic effect to induce photocurrent. (d) Fabricate additional layer of MOS to suppress charge recombination.

molecules are stimulated to form electrons. The electrons are then injected into the photoanode's semiconductor conduction band (CB) and transmitted via an external circuit to the counter electrode with the help of an electrolyte. This mechanism repeats itself as long as the cell is illuminated. Titanium dioxide (TiO_2) is an excellent photoanode material due to its physicochemical properties [1,2]. It has good thermal stability [3], photochemical strength [4], relatively low toxicity [5], and a different bandgap for each of its crystallographic phases, namely anatase (3.2 eV) [1], rutile (3.0 eV) [6], and brookite (3.4 eV) [7,8].

Anatase TiO_2 has the highest photocatalytic activity and electron mobility, is metastable, and easily transforms into rutile at high temperatures [9,10]. Rutile TiO_2 is more workable due to its chemical stability and remarkable light-scattering capabilities for effective light absorption [11]. TiO_2 does present a hurdle, given that its absorption band is in the ultraviolet region and its low electrical conductivity due to an abundance of interparticle interfaces [12–14]. Previous studies determined that a good photoanode should have a large surface area for dye trapping, high surface roughness to absorb or scatter light, and good electron acceptance [12,13]. Therefore, strategies such as ion doping [15,16], morphology modification [17], decoration with noble metals

for plasmonic effect and additional layer with metal oxide materials [18, 19] have been investigated to enhance the electronic and structural properties of TiO_2 as illustrated in Fig. 1.

Palomares et al. reported that adding metal oxide layers improved photon-generated carrier injection and collection at the TiO_2-dye interface [20]. The metal oxide layers are conventionally composed of binary oxides such as Zinc oxide (ZnO) [21,22], tin oxide (SnO_2) [23, 24], ceria (CeO_2) [20,25] and niobium pentoxide (Nb_2O_5) [14,26]. Recently, ternary oxides have gained popularity since they provide a larger scope for tweaking physical-chemical properties than binary oxides. Aravinthkumar et al. revealed that a $SrTiO_3$ ternary oxide layer produced a higher photovoltage with its more numerous photocatalytic active sites [27]. Saadat et al. found that Zn_2SnO_4 has high electron mobility and electrical conductivity [28], while Purushotham Reddy et al. concluded that $BaSnO_3$ facilitates the electron transport layer in DSSC [29]. Strontium Stannate, $SrSnO_3$, has an orthorhombic perovskite structure and demonstrated excellent electrical conductivity with respect to the FTO and better absorption of incident light [30–32].

Ion doping and additional metal oxide layer can boost DSSC photoanode electrical performance and optical bandgap. By these strategies, the unabsorbed photon-electron in the structure of TiO_2 photoanode can be scattered and reflected to prevent electron loss. Moreover, applying 3D nanoflower morphology can be advantageous for surface area enhancement. This is because nanoparticle can only scatter small amount of visible light due to the smaller grain size. Hence, light irradiation is easily passing through the photoanode layer without interacting with dyes molecule and less photo-current is generated [33]. In addition, nanoflower morphology with additional metal oxide layer also can hurdle the light to pass through due to opaque cell. Thus, adding up with ion doping of noble metal may create surface plasmon resonance inside the cell.

The present study explored the effect of doping and additional metal oxide layer on the structure of rutile TiO_2 nanoflower (rT-NF). The rT-NF was doped with different concentrations of silver (Ag) via the hydrothermal method. $SrSnO_3$ was plasma deposited on the surface. This unique combination aimed to overcome the TiO_2 photoanode's limited surface area, narrow visible photoresponse bandwidth, and low electron mobility. The combination of the rutile phase and perovskite should widen the absorption band and enhance the photoresponse significantly. RF sputtering was employed to decorate the rT-NF surface with thin perovskite nanoparticles. The $SrSnO_3$-enhanced Ag-doped rT-NF and non-$SrSnO_3$-enhanced rT-NF were compared in terms of their structural, morphological, topological, optical, and electrical properties to highlight the potential of this new approach in improving the material's photoanode optoelectronic performance.

2. Experimental method

2.1. Materials

Hydrochloric acid (HCl, 36%–38% purity, J. T. Baker, Thailand), titanium (IV) butoxide (Ti(OBu)₄, 97% purity, Sigma Aldrich, China), silver nitrate (AgNO₃) (QRëC, New Zealand), and DI water was used as the hydrothermal precursors. The 99.9% pure $SrSnO_3$ target (Plasmaterials Inc, California) was used as the coating, while 99.99% pure Ag target (iTASCO, Korea) was used for metal contact. Fluorine-doped tin oxide (FTO) on glass substrates with resistivity ~8 Ω/cm and sample dimensions 2.0 cm × 1.5 cm; (Solaronix, Switzerland) was used as a transparent conductive substrate.

2.2. Preparation of Ag-doped rT-NF using hydrothermal method

Ag-doped rT-NF was prepared via the hydrothermal method [34]. The 2.0 cm × 1.5 cm FTO-glass substrate was cleaned with acetone, ethanol, and DI water in an ultrasonic bath for 10 min each. In a clean beaker, 80 mL of HCl and 80 mL of DI water were combined and stirred
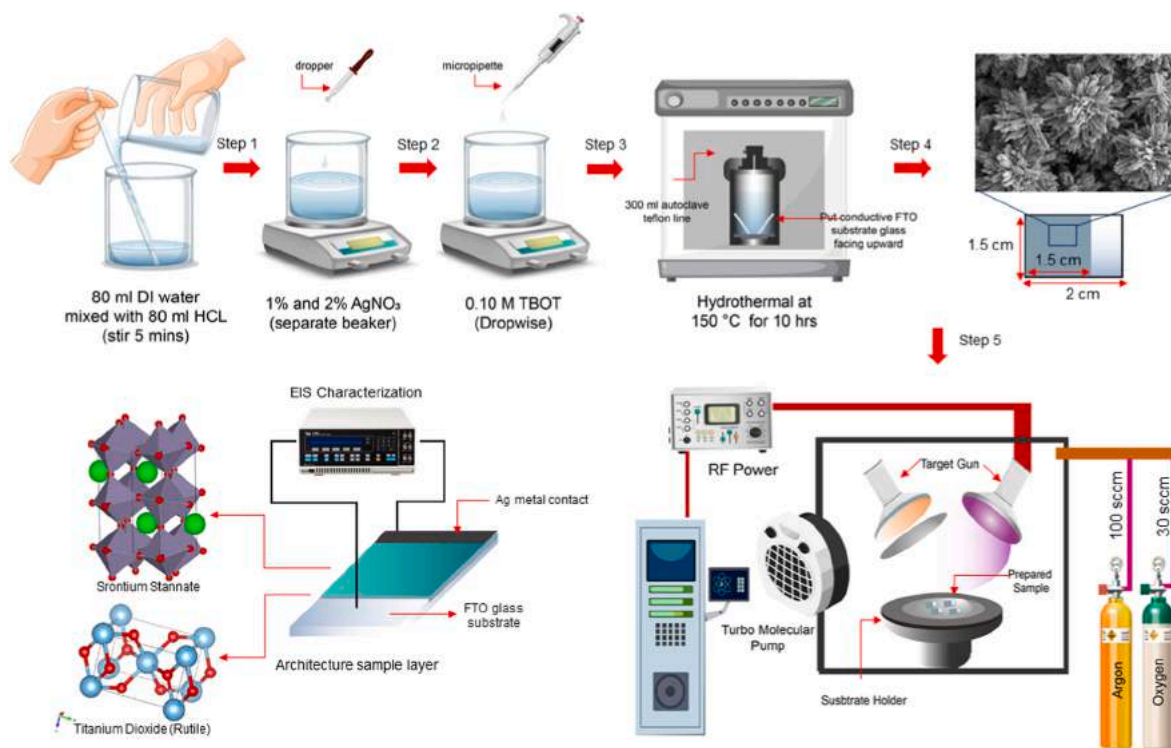
Fig. 2. Preparation method.

Table 1
Sample labelling.

Sample Name	Ag dopant concentration	Time Deposition SrSnO$_3$
S1Ag 10 min	1%	10 min
S1Ag 30 min	1%	30 min
S2Ag 10 min	2%	10 min
S2Ag 30 min	2%	30 min

for 5 min at a constant speed (Fig. 2, Step 1). AgNO$_3$ was added at different weight percentages (1% and 2% of AgNO$_3$), and the mixture was stirred for 30 min (Fig. 2, Step 2). Then, 0.10 M of Ti(OBu)$_4$ was added dropwise using a micropipette, stirring the solution until it turned transparent (Fig. 2, Step 3). The solution was carefully transferred to 300 mL autoclaves that contained FTO-glass substrates, with the FTO layer facing up. The autoclaves were sealed, then baked for 10 h at a constant temperature of 150 °C for rT-NF growth. After the growth was complete, the samples were rinsed with DI water several times and dried at room temperature. The samples of rT-NF doped with 1% Ag and 2% Ag were designated as S1Ag and S2Ag, respectively.

2.3. Radio-frequency magnetron sputtering

SrSnO$_3$ was deposited onto the Ag-doped rT-NF samples using magnetron sputtering in the radio frequency (RF) mode at 100 W discharge powers (Fig. 2, Step 5). The main chamber was evacuated to a base pressure of 7.7×10^{-6} Torr. Pre-sputtering cleaning was performed for 30 min in pure argon gas to remove contaminants from the SrSnO$_3$ target. The SrSnO$_3$ target was positioned at the top of the chamber while the samples were placed on sample holders 14 cm away from the target. Argon flow rate was set to 100 sccm to achieve the working pressure of 5 mTorr during the deposition process. The sample holder was rotated at 5 rpm for better uniformity. The 1% and 2% Ag-doped rT-NF samples were coated with SrSnO$_3$ for 10 min and 30 min in two separate processes to evaluate the effect of different coating thicknesses on light scattering performance. After that, silver was sputtered onto the samples

for 60 min to form the metal contact for electrical impedance spectroscopy (EIS) measurement (Fig. 2). The sample labelling for identification is tabulated in Table 1.

2.4. Characterization tools

The structure and crystallinity of the prepared Ag-doped rT-NF and Ag-doped rT-NF/SrSnO$_3$ samples were analyzed using X'Pert PAN-alytical X-ray diffraction (XRD) with Cu κ_α radiation, $\lambda = 1.54$ Å at 2θ angle from 20° to 80°. Crystallite size was calculated using the Debye-Scherrer method based on the X-ray diffraction spectra [35,36].

$$D = \frac{K\lambda}{\beta \cos \theta} \tag{1}$$

$$\delta = \frac{\beta \cos \theta}{4} \tag{2}$$

$$\varepsilon = \frac{1}{D^2} \tag{3}$$

D is crystallite size, λ is wavelength, β is the full width at half maximum (FWHM) of each peak, and θ is Bragg's diffraction angle. Additionally, particle interconnectivity, dislocation density (δ) and microstrain (ε) were calculated to evaluate sample quality.

Sample surface morphology was observed using a field-emission scanning electron microscopy (FESEM) (JSM-7600F, JEOL, Japan) at × 50k magnification and was operated at an accelerating voltage of 5 kV. Absorbance spectra were recorded on the prepared samples using Ultraviolet–visible spectroscopy (UV–Vis) (UV-1800, Shimadzu Corporation, Japan). The prepared samples' spectral responses were analyzed with a Spectrum Measurement System (PEC-S20, Peccal, Japan) with wavelength between 300 and 1200 nm, DC, and a 300 W xenon arc lamp as the light source. The IPCE was derived from EQE tested under ambient atmosphere. Surface topology and roughness of sample were analyzed using Atomic Force Microscopy, AFM (XE-100, Park System, Korea), in the non-contact mode. A microRaman spectroscope (Horiba Xplora Plus, USA) equipped with a 532 nm laser source and an
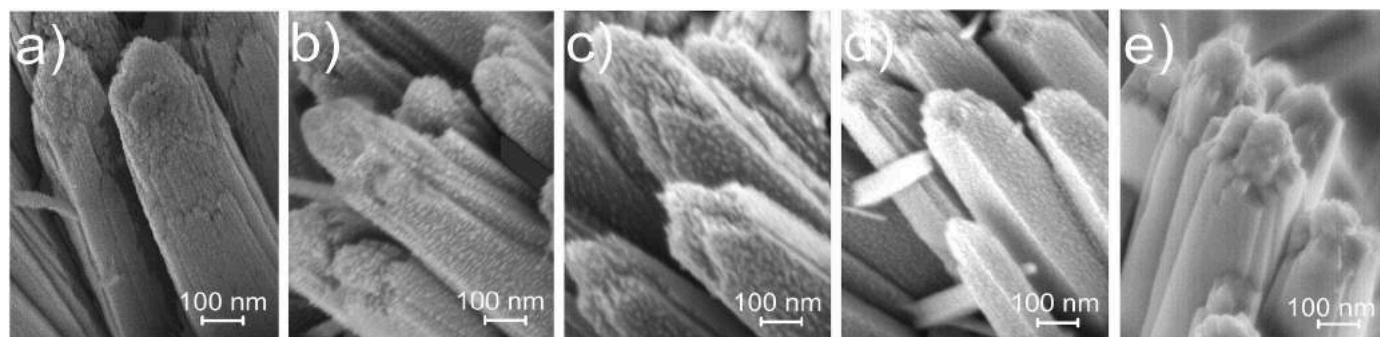
Fig. 3. FESEM (a) rT-NF, (b) S1AG 10 min, (c) S1AG 30 min, (d) S2AG 10 min (e) S2AG 30 min.
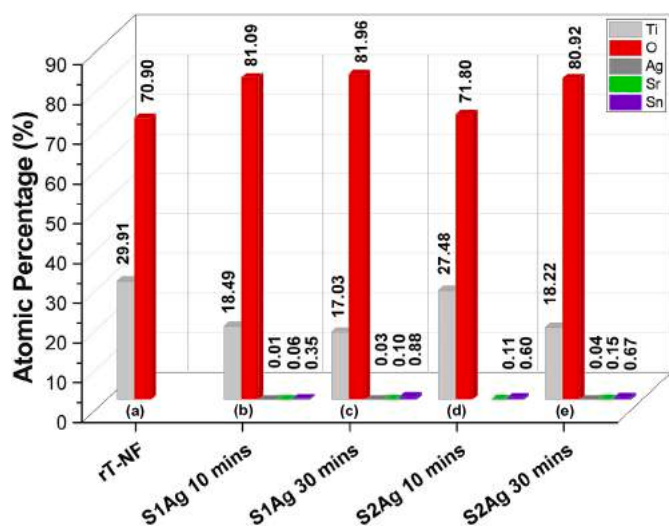

Fig. 4. EDS (a) rT-NF, (b) S1AG 10 min, (c) S1AG 30 min, (d) S2AG 10 min (e) S2AG 30 min.

Fig. 5. Raman spectral data.

electrically refrigerated charged-coupled device (CCD) camera was used to investigate the sample's structure. The Lakeshore Model CPX Cryogenic Probe Station and Keysight Agilent B1500A semiconductor device parameter analyzer (USA) was used to sweep the sample dark current-voltage (I–V) measurement between 2 and −2 V to identify I–V characteristic. Electrical characterization was performed using an impedance/gain-phase analyzer (Solartron 1260, Keysight Technologies, USA), wielding an AC signal 10 mV in amplitude and 1 kHz to 1.5 MHz in frequency.

3. Results and discussions

3.1. Morphology

Fig. 3 shows the FESEM images of rT-NF, S1AG 10 min, S1AG 30 min, S2AG 10 min and S2AG 30 min. Hamed et al. stated that the rod-petal structure typical in nanoflowers provides a direct path for electrons that reduces electron-hole recombination on the surface of TiO_2 [34]. Nanoflowers also have a large active surface area that improves photon absorption, as demonstrated by prior work by N. Desai et al. [35]. FESEM images revealed that the sides of the TiO_2 nanoflower petal were coated with a dispersion of nanoparticles, presumably $SrSnO_3$ particles. Fig. 3(b–d) show that the nanoflower sides are rougher than bare TiO_2. Fig. 3(e) displays that S2AG 30 min, the most Ag-doped TiO_2 sample, exhibited a distinct surface morphology where the sides are smoother than any other sample and are inferred to be coated with a hetero TiO_2–$SrSnO_3$ structure due to lengthy deposition.

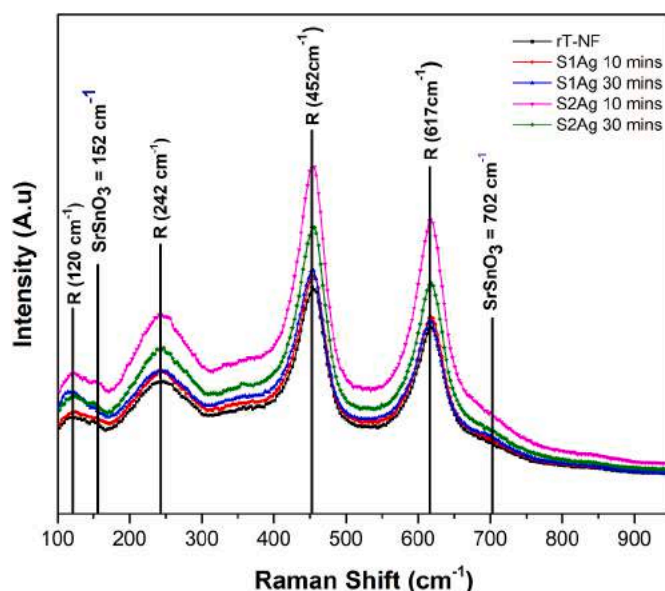The crystal structure of TiO_2 could be anatase, rutile (as reported this

work), or brookite phases. Each of these structures has a distinct crystal lattice, which determines the physical and chemical properties of the sample. In this study, the TiO_2 rutile nanoflower sample appears larger needle crystals which is more than 500 nm in length is attributed to the monocrystalline structure. The crystal lattice of the needle crystals nanoflower morphology could grow during the hydrothermal reaction, which is depending on temperature reaction or time reaction. In this study, the 150 °C constant temperature for 10 h led to preferentially nucleation growth of larger needle crystals nanoflower in orientations of (101) and (111) plane. The confirmation presence of TiO_2 and $SrSnO_3$ also is evaluated by EDS analysis in Fig. 4. Although the atomic level of element Sr and Sn is significantly lower than the desired stoichiometry, the corresponding pattern shows the presence of $SrSnO_3$ on the surface TiO_2. The highest Sn (0.88 wt%) found in the S1Ag 30 min sample. This EDS analysis confirmed the Ti and O atomic element exist in all sample and Sr, Sn and O element in sample S1Ag (10 min and 30 min) and S2Ag (10 min and 30 min). Owing to the high sensitivity and limited detection capability of EDS, detecting Ag dopant in low concentrations can be challenging. The confirmation of the presence of Ag dopant is ascertained through XPS analysis in our previous work [34].

3.2. Raman Spectroscopy

Raman spectroscopy analysis revealed the sample's local structural disorder and crystal quality (Fig. 5). rT-NF has a tetragonal structure with a P42/mnm space group, giving it four Raman active vibrational

Table 2
Raman spectral data of rT-NF and SrSnO$_3$compared to previous works.

	M.M.I. Megat Hasnan et al. [6]	H.L. Ma et al. [37]	M.C.F. Alves et al. [38]	This Research
rT-NF	105 cm^{-1}	140 cm^{-1}	–	120 cm^{-1}
	236 cm^{-1}	235 cm^{-1}	–	242 cm^{-1}
	445 cm^{-1}	445 cm^{-1}	–	453 cm^{-1}
	609 cm^{-1}	609 cm^{-1}	–	617 cm^{-1}
SrSnO$_3$	–	–	151 cm^{-1}	152 cm^{-1}
	–	–	703 cm^{-1}	702 cm^{-1}

modes: B$_{1g}$, E$_g$, A$_{1g}$, and B$_{2g}$. Raw and Ag-doped SrSnO$_3$-coated rT-NF exhibited dominant peaks at 120 cm^{-1}, 242 cm^{-1}, and 617 cm^{-1}, corresponding to the B$_{1g}$, E$_g$, and A$_{1g}$ rutile phase modes, respectively. The results agreed with previous works (Table 2), confirming the formation of the TiO$_2$ rutile phase. The post-deposition of SrSnO$_3$ particles on Ag-doped rT-NF through RF sputtering had increased the material's Raman intensity, which correlates with thickness of sample accordance deposition time of SrSnO$_3$.

3.3. Topology

Atomic force microscopy (AFM) images of the prepared samples (Fig. 6) were used to determine the surface roughness by root-mean-square (RMS) with a scan size of 10 μm × 10 μm. The surface roughness of photoanode electrodes reportedly has a crucial role in electron transport because it influences the contact area between the photoanode and the dye molecules [39]. The surface roughness of the photoanode has been found to significantly affect the interfacial properties between the dye and the semiconductor photoanode, as it increases the surface area available for dye adsorption and improves the contact between the dye and the semiconductor photoanode. This results in an increase in the efficiency of electron injection from the dye to the semiconductor photoanode and a reduction in the recombination rate of photo-generated electron-hole pairs. A rougher surface leads to a higher specific area, thereby enhancing light-scattering and facilitating the trapping of more dye [40]. While Gnida et al. claimed that the thickness of the additional layer did not affect the roughness of the TiO$_2$ [41], it does affect the light absorption intensity, which we will study using UV–Vis spectroscopy.

An excessively thick photoanode layer may absorb less light since it acts as a physical barrier that hinders light from reaching the dye molecules. The thicknesses of the prepared samples, rT-NF, S1Ag 10 min, S1Ag 30 min, S2Ag 10 min, and S2Ag 30 min, were 19.72 μm, 28.39 μm,

30.61 μm, 41.99 μm, and 42.90 μm, respectively. rT-NF had an RMS roughness of 24.95 nm (Fig. 6(a)). After being deposited with 10 min of SrSnO$_3$ on S1Ag, its RMS roughness increased to 28.39 nm (Fig. 6(b)), while a 30-min deposition of SrSnO$_3$ on S1Ag resulted in an RMS roughness of 31.19 nm (Fig. 6(c)). For S2Ag 10 min, the RMS roughness was 29.73 nm (Fig. 6(d)), and the RMS roughness for S2Ag with 30 min deposition of SrSnO$_3$ was 32.32 nm (Fig. 6(e)).

Surface roughness is also influenced by the RF power used in the sputtering [42,43]. The RF source utilized capable of generating plasma in between electrodes and inducing produces Ar$^+$ ions which can result a rougher surface if the deposition rate is not adequately controlled. An elevated RF power in the deposition process may result increased sample surface compaction, induce compressive stress, and cause significant modifications on the sample surface [44]. The energy of the ions may also be enhanced, resulting in an increase in the ion bombardment on the sample surface. This process can lead to the roughening of the surface. Furthermore, high-energy ions may cause re-sputtering, which involves the ejection of previously deposited material from the surface, leading to a rougher surface. Therefore, the use of higher RF power during the sputtering process resulted in a roughened surface and an increased surface area allowing for a greater quantity of dye-sensitizer to adhere to the sample surface. From this observation, it is critical to research the optimum roughness and thickness of photoanode electrodes for light absorption.

3.4. Structural and elemental analysis

XRD is an important technique in material science used to investigate the sample crystallinity structure, phase transition, and material purity [4]. Fig. 7(a) shows the XRD diffraction pattern of intrinsic rT-NF and Ag doped rT-NF with SrSnO$_3$ (S1Ag 10 min, S1Ag 30 min, S2Ag 10 min, and S2Ag 30 min).

All observed peaks agreed with ICDD card No. 98-003-9167, which confirmed the tetragonal rutile phase of rT-NF, and ICDD card No. 98-026-1491, which confirmed the orthorhombic structure of strontium stannate (IV) (O$_3$Sn$_1$Sr$_1$). The peaks of both rutile phases for the uncoated and coated samples (rT-NF and Ag doped-rT-NF with SrSnO$_3$, respectively) agreed well with previous works [6,32,34]. The incorporation Ag dopant with perovskite SrSnO$_3$ in rutile TiO$_2$ lattice by de-convolution technique shows shifting in diffraction peaks in Fig. 7(b and c). The broadening of diffraction peaks in Fig. 7(b and c) indicates the incorporation of Ag, Sr, and Sn atoms in the TiO$_2$ lattice, a consequence of the resulting strain effects from different crystal structures.
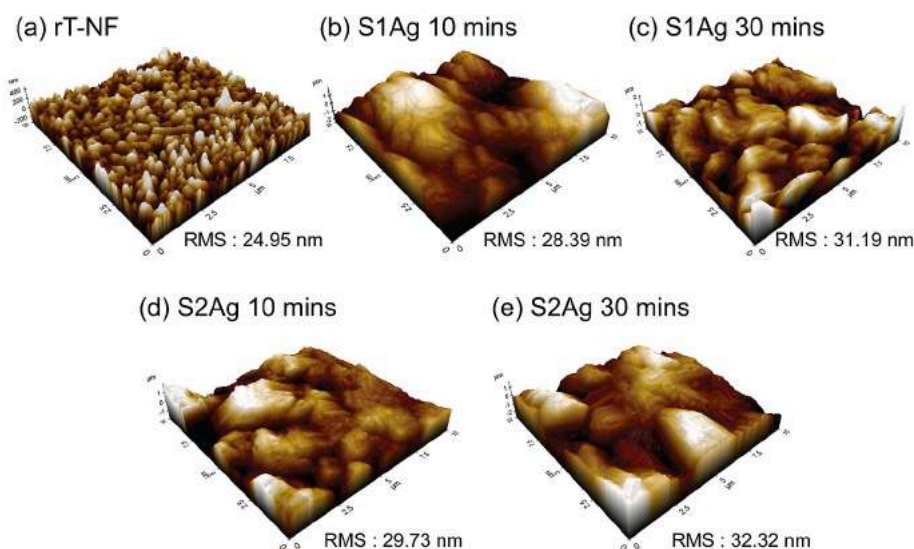

Fig. 6. AFM Topology of (a) rT-NF (b) S1Ag 10 min (c) S1Ag 30 min (d) S1Ag 30 min and (e) S2Ag 30 min.
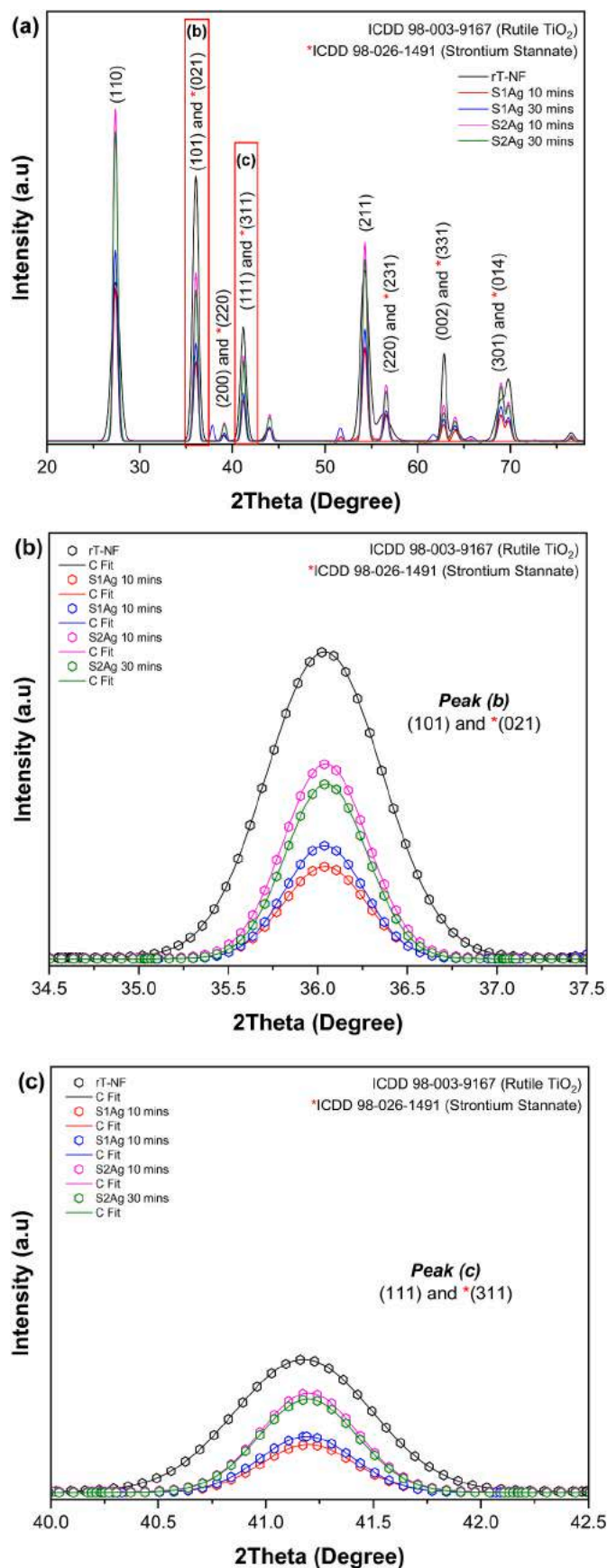
Fig. 7. (a) XRD diffraction pattern of rT-NF, S1Ag (10 min and 30 min) and S2Ag (10 min and 30 min) (b) De-convolution Peak (110) plane (c) De-convolution Peak (111) plane.

Furthermore, the intensity values of the diffraction peaks of (021) and (311) planes were lower than that of (101) and (111) planes. This phenomenon can be attributed to the aggregation of metal ions in the sample lattice, resulting in the low-intensity value of the diffraction peaks of (021) and (3111). Previous work suggests that the aggregation of metal ions with a larger radius and a smaller ionic radius will cause a shift in the diffraction peak to the higher angle [45].

However, no diffraction peak for Ag and its oxides was detected in Ag-doped rT-NF with $SrSnO_3$, confirming that the doping did not interfere with the rutile phase. This result also indicated that the samples were in good rutile phase crystallinity and were inferred to contain $SrSnO_3$ particles dispersed on the surface of the TiO_2 nanoflower structure [4,34]. Furthermore, it should be noted the small amount of Ag dopant cannot be defined by the accuracy of X-ray diffraction. Noble metal included Ag able to enhance light-scattering which is crucial for light harvesting [46].The Ag dopant also introduces an oxidation state into the rT-NF catalyst, which acts as an electron trap, reducing the recombination between the electron–hole pair and broaden light absorption area. Studies have shown that plane (111) and plane (110) contain high-energy facets where oxidative and reductive sites trap photoholes and electrons [47,48]. Electron is highly mobile in the rutile phase, which means they can move to the surface and react with the dye-sensitizer at planes (111) and (110). The effect of sample after incorporating Ag dopant and coated with $SrSnO_3$ was further analyzed under the influences of the strain and crystal imperfections of full width at half maximum (FWHM) by using Williamsons-Hall (W–H) method after de-convolution diffraction peak as following equation (4):

$$\frac{\beta \cos \theta}{\lambda} = \frac{1}{D} + \frac{\varepsilon \sin \theta}{\lambda} \tag{4}$$

where β is FWHM, θ is the diffraction angle, λ is the x-ray wavelength, D is the average crystallite size and ε is the effective strain or stress. The strain was determined through calculating the slope (m), while the average crystallite size was determined by taking the inverse of the intercept of the linear fit as shown in Fig. 8.

Dislocations can occur in a crystal lattice due to defects in the lattice planes, leading to areas of tensile strain. In the case of the rT-NF sample, the W–H plot indicates a lattice with an ε value of 1.95×10^{-3} and an average D value of 11.84 nm. However, after coating the rT-NF with $SrSnO_3$, the W–H plot shows a compressed lattice, with ε values of 5.78×10^{-4}, 6.58×10^{-4}, 6.58×10^{-5}, and a negative slope of -1.39×10^{-4} (S1Ag 10 min, S1Ag 30 min, S2Ag 10 min, and S2Ag 30 min, respectively), along with D values of 17.40 nm, 17.64 nm, 15.27 nm, and 15.02 nm, respectively. The W–H plot suggests that the high strain observed in the intrinsic rT-NF sample may be due to defects that occurred during the nucleation and growth of the nanoflower in the hydrothermal reaction. However, the substitution of Ag dopant and Sr–Sn–O bond appears to reduce the tensile strain in the rT-NF sample. This is because these processes distort the crystal structure and cause implications on its unit cell structure to diverge from its ideal stoichiometry. As shown in Table 3, the high dislocation density observed in the rT-NF sample is attributed to this distortion, as compared to the coated $SrSnO_3$ sample.

3.5. Optical properties

The samples were analyzed via UV–Visible spectroscopy in the 400–700 nm wavelength range. The absorption edge in the 424–445 nm range (Fig. 9(a)) indicated visible light absorption, in agreement with previous work [49]. Visible light absorption is a desirable trait required for the dye-sensitizer molecules to stimulate the photon on the photoanode surface and drive the DSSC mechanism. The optical bandgap energy (E_g) was estimated via the Tauc method by plotting the straight-line portion of $(\alpha h\nu)^2$ against the photon energy ($h\nu$) by using absorbance value [14,50]. Accordingly, the E_g relationship with the
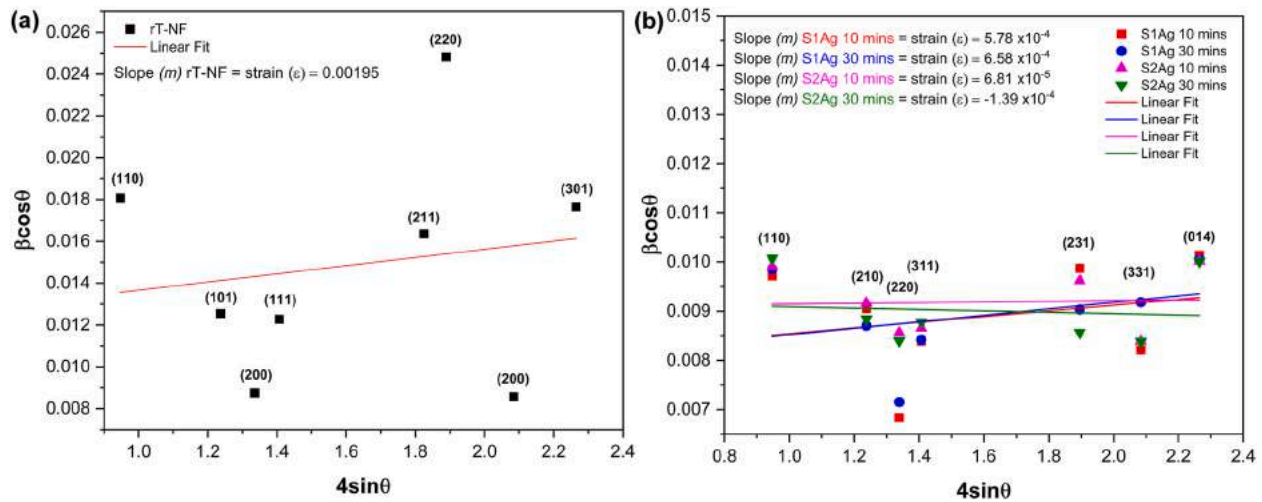
Fig. 8. The Williamsons–Hall (W–H) plot. (a) rT-NF, (b) S1Ag (10 min and 30 min) and S2Ag (10 min and 30 min).

Table 3
Values for crystallite size (D), dislocation density (δ) and microstrain (ε) from XRD analysis.

Sample	HKL	2Theta (Degree)	FWHM (Degree)	Crystallite Size, D, (nm)	Dislocation density, δ,(nm^2)	Micro strain, ε
rT-NF	(110)	27.39	1.065	8.01	15.57	8.97
	(101)	36.03	0.756	11.53	7.51	4.53
	(200)	39.00	0.532	16.54	3.65	2.86
	(111)	41.17	0.751	11.79	7.19	3.74
	(211)	54.27	1.053	8.84	12.77	3.30
	(220)	56.35	1.613	5.83	29.38	4.68
	(200)	62.82	0.575	16.88	3.50	1.28
	(301)	68.96	1.227	8.20	14.86	2.05
S1Ag 10 min	(110)	27.38	0.573	14.90	4.50	4.82
	[a](021)	36.04	0.545	15.99	3.90	3.27
	[a](220)	39.10	0.415	21.17	2.23	2.23
	[a](311)	41.19	0.513	17.25	3.35	2.56
	[a](231)	56.58	0.642	14.66	4.64	1.84
	[a](331)	62.78	0.551	17.63	3.21	1.23
	[a](014)	68.95	0.704	14.28	4.90	1.18
S1Ag 30 min	(110)	27.38	0.581	14.69	4.63	4.89
	[a](021)	36.03	0.524	16.63	3.61	3.14
	[a](220)	39.12	0.434	20.24	2.44	2.33
	[a](311)	41.19	0.515	17.20	3.37	2.56
	[a](231)	56.57	0.587	16.03	3.89	1.69
	[a](331)	62.78	0.616	15.77	4.02	1.38
	[a](014)	68.95	0.698	14.40	4.81	1.17
S2Ag 10 min	(110)	27.39	0.584	14.62	4.67	4.91
	[a](210)	36.04	0.552	15.80	4.00	3.31
	[a](220)	39.11	0.520	16.91	3.49	2.79
	[a](311)	41.19	0.529	16.72	3.57	2.64
	[a](231)	56.57	0.626	15.05	4.41	1.80
	[a](331)	62.79	0.563	17.26	3.35	1.26
	[a](014)	68.97	0.696	14.45	4.78	1.16
S2Ag 30 min	(110)	27.39	0.594	14.37	4.84	5.00
	[a](210)	36.04	0.532	16.37	3.72	3.19
	[a](220)	39.11	0.510	17.23	3.36	2.74
	[a](311)	41.19	0.537	16.50	3.67	2.67
	[a](231)	56.57	0.557	16.90	3.49	1.60
	[a](331)	62.79	0.562	17.27	3.35	1.26
	[a](014)	68.97	0.695	14.46	4.78	1.16

[a] Strontium stannate (IV) (O$_3$Sn$_1$Sr$_1$).

absorption coefficient, *a*, is given by the equation:

$$a = \frac{A \left(hv - E_g\right)^n}{hv} \tag{5}$$

Here, $a = (2.303 \times Absorbance \times Energy)^2$, is the incident photon energy where $hv = 1240/wavelength$, *A* is an energy-independent constant,

and for direct bandgap energy, $n = 2$. In other words, light is weakly absorbed in materials with a low absorption coefficient.

Adding SrSnO$_3$ coating and Ag ion doping to the rT-NF resulted in an infinitesimal change in the optical bandgap for all samples (Fig. 9(b)). The rT-NF gained 3.0 eV of bandgap, which agreed with another work on rutile TiO$_2$ [35]. Bandgap energy calculation revealed an overall reduction for the Ag-doped and SrSnO$_3$-coated samples. This was due to
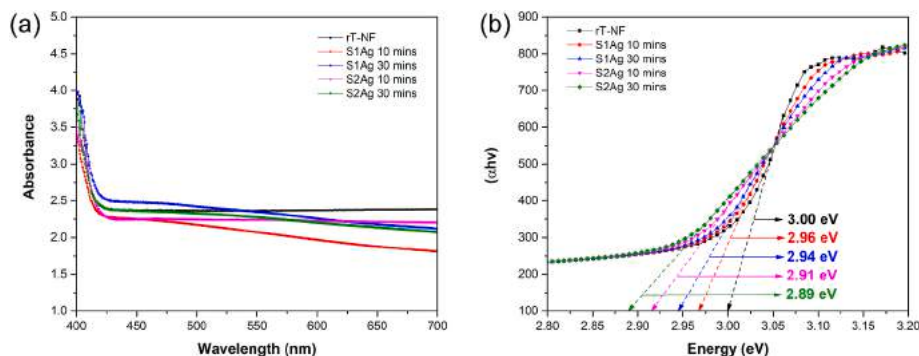
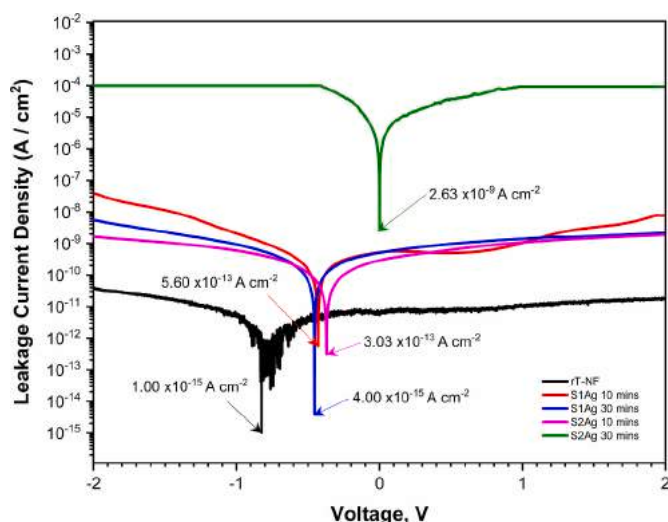**Fig. 9.** UV–vis spectroscopy of (a) absorbance (b) optical bandgap.
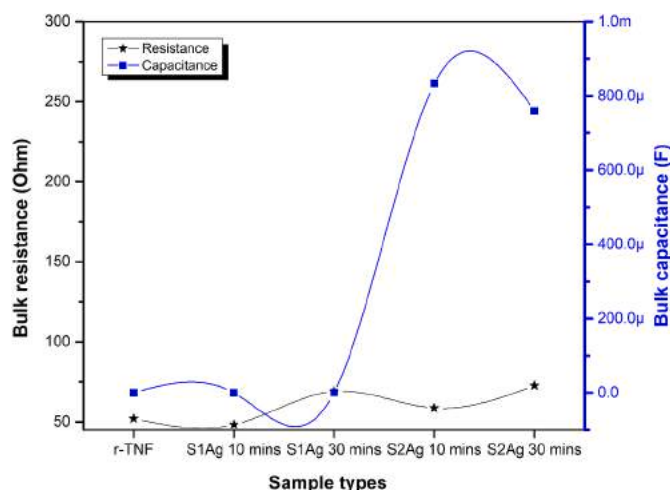

Fig. 10. I–V of leakage current.

Fig. 12. Bulk resistance and bulk capacitance of the samples extracted from Nyquist plot fitting.

increase in absorbance and reduction in the optical bandgap of S1Ag and S2Ag samples, each with different deposition times of 10 and 30 min, can be attributed to SPR. This effect allows Ag to absorb high-energy photons and convert them into lower-energy photons, thereby reducing the energy bandgap. In this study, the optical bandgap values were observed to decrease to 2.96 eV, 2.94 eV, 2.91 eV, and 2.89 eV for S1Ag (10 min and 30 min) and S2Ag (10 min and 30 min), respectively as shown in Fig. 9(b).

3.6. Electrical properties

To evaluate the effect of Ag dopant and perovskite $SrSnO_3$ coating, current-voltage (I–V) analysis was conducted using Semiconductor Device Parameter Analyzer with applied voltage between −2 V and 2 V. Fig. 10 shows the I–V characteristic of the samples rT-NF, S1Ag (10 min and 30 min), and S2Ag (10 min and 30 min). The current, I, at 0 bias was approximately below the magnitude of 10^{-7}, and the curve was shifted to reverse bias leakage current for most of the samples except for S2Ag 30 min This deviated slightly from the leakage current characteristic with a symmetrical curve at 0 V resembling a p-n junction.

EIS was used to further evaluate the electrical properties of the photoanode electrode interfaces, as shown in the Nyquist plot (Fig. 11). EIS was performed for all prepared samples at V_{OC} bias in dark condition at room temperature. Measurements were taken in the 1 kHz to 1.5 MHz frequency range with 1 V peak-to-peak AC applied. The results were fitted using Gamry software with an equivalent circuit shown in Fig. 11. The series resistance (R_s) describes the resistance of the bulk sample, while the contact resistance (R_{ct}) represents the contact resistance of Ag.
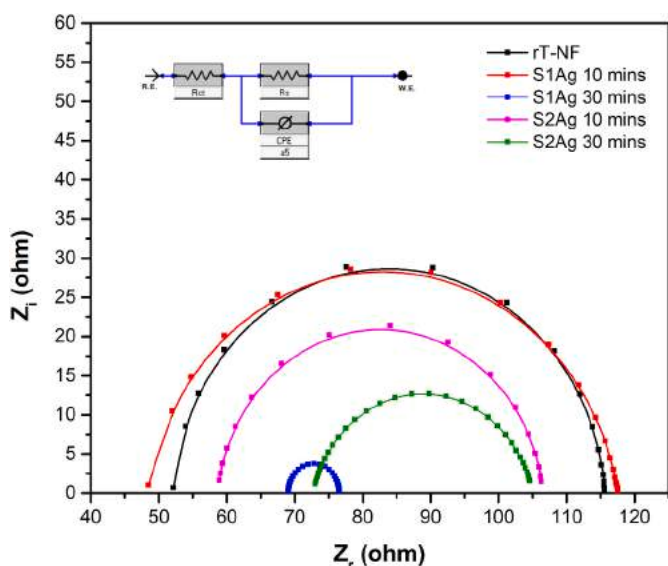

Fig. 11. Nyquist plot of the samples.

the surface plasmon resonance (SPR) of the particles caused by electromagnetic field interference with the conduction electrons of Ag and $SrSnO_3$ distributed in the TiO_2 matrix [51]. The phenomenon of SPR arises when the oscillating electrons of noble metal Ag absorb energy from the incident light, leading to a shift towards the visible region. This
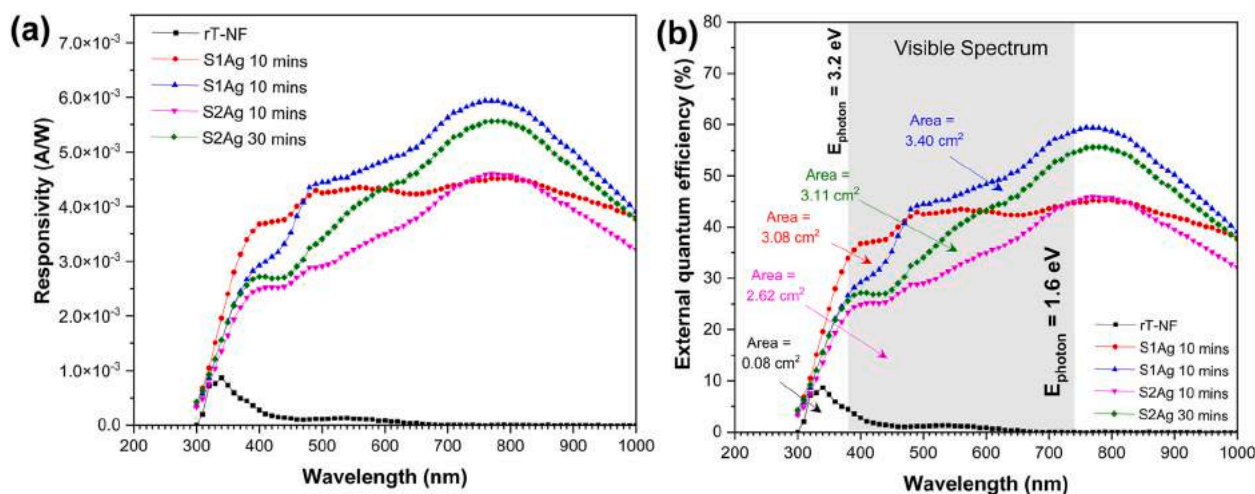
Fig. 13. Photoresponse (a) responsivity (b) EQE (%).

Table 4
Photoresponse area under curve and max photo response.

Sample	Optical	Electrical				Photoresponse	
	Thickness, T (μm)	Roughness, (nm)	Bandgap, (eV)	R_s (Ω/cm^2)	C (F)	Area under curve (cm^2)	Max Photo response (A/W)
rT-NF	19.72	24.95	3.00	52.11	1.96×10^{-8}	0.08	1.0×10^{-3}
S1Ag 10 min	28.39	28.39	2.96	52.25	1.66×10^{-8}	3.08	4.2×10^{-3}
S1Ag 30 min	30.61	31.19	2.94	7.51	5.64×10^{-7}	3.40	6.0×10^{-3}
S2Ag 10 min	41.99	29.73	2.91	43.90	8.33×10^{-4}	2.62	4.5×10^{-3}
S2Ag 30 min	42.90	32.32	2.89	32.39	7.59×10^{-4}	3.11	5.5×10^{-3}

The EIS study measured a sample's bulk resistance and bulk capacitance to elucidate the effect of post-deposition time on electrical properties.

S1Ag 30 min attained the smallest semicircle of bulk $R_s < R_{ct}$ (7.51 Ω < 69.52 Ω) followed by S2Ag 30 min, $R_s < R_{ct}$ (32.39 Ω < 72.68 Ω) and S2Ag 10 min, $R_s < R_{ct}$ (43.90 Ω < 61.66 Ω). For the rT-NF and S1Ag 10 min samples, R_{ct} was bigger than R_s with (63.52 Ω > 52.11 Ω) and (67.52 Ω > 52.25 Ω), respectively. The result indicated that the Ag dopant and SrSnO$_3$ coating accelerated electron transport in the interfacial TiO$_2$. The modelled capacitance (*C*) calculated by the circuit in the Nyquist plot of Z_r/Z_i resulted from charge accumulation on the electrode surface. Fig. 12 shows the capacitances for rT-NF, S1Ag 10 min, S1Ag 30 min, S2Ag 10 min, and S2Ag 30 min being 1.96×10^{-8} F, 1.66×10^{-8} F, 5.64×10^{-7} F, 8.33×10^{-4} F, and 7.59×10^{-4} F, respectively. In this context, a higher *C* implies a higher effective surface area for the photoanode electrode.

3.7. Photoresponse

The responsivity magnitudes between 300 and 1000 nm were investigated (Fig. 13) to derive the absorbance results. In Fig. 13(a), rT-NF exhibited response under illumination within 300–350 nm, whereas Ag-doped and SrSnO$_3$-coated rT-NF continued to absorb to at least 1000 nm, contributing to the broad spectral light harvesting, which was in good agreement with its UV–vis spectrum. The high photoresponse was attributed to the charge carriers generated upon photoexcitation, leading to the generation of free electrons in the semiconducting layer. In the photovoltaic mechanism, visible light photons have energy between 3.2 eV (violet region, $\lambda = 380$ nm) and 1.6 eV (red region, $\lambda = 740$ nm) (Fig. 13(b)). Thus, the material's bandgap energy should be higher than the visible photon energy for electrons to migrate from the valence band to the conduction band. External quantum efficiency (EQE) indicates the amount of photon that can be absorbed for electron excitation. S1Ag 30 min exhibited the highest photoresponse at 740 nm with an active area under the curve of 3.40 cm^2. The findings are tabulated in

Table 4, wherein the SrSnO$_3$ post-deposition on Ag-doped TiO$_2$ nanoflower can optimize the optoelectronic performance of rT-NF.

4. Conclusion

The present work utilized the hydrothermal (wet chemical) method to synthesize TiO$_2$ NF, doping for bandgap reduction, and RF sputtering to deposit additional SrSnO$_3$ layers on the rT-NF for DSSC photoanode enhancement. The Ag doping and the embedded SrSnO$_3$ layer in the S1Ag (10 min and 30 min) and S2Ag (10 min and 30 min) samples successfully reduced the energy bandgap to below 3.0 eV, while also tuning the wavelength to the visible spectrum as validated by the responsive spectra above 400 nm under illumination. The smallest circle Nyquist plot representing the bulk resistance for S1Ag 30 min indicated that embedded SrSnO$_3$ could improve the properties of bare TiO$_2$ by facilitating photon absorption under illumination.

Authorship contribution statement

N.N. Ishak: Writing, formal analysis, investigation. **N. Nayan:** Funding acquisition, theoretical study, supervision. **M.M.I. Megat Hasnan:** Theoretical analysis, data curation. **N.K.A. Hamed:** Hydrothermal method. **Y. Md Yunos:** Funding acquisition, article editing. **M. S. Mohamed Ali:** Conceptualization, supervision, validation, writing, editing and funding acquisition.

CRediT authorship contribution statement

Nurul Najihah Ishak: Formal analysis, Investigation, and writing. **Nafarizal Nayan:** Funding acquisition, theoretical study, Supervision. **Megat Muhammad Ikhsan Megat Hasnan:** Theoretical analysis, Data curation. **Noor Kamaliah Abd Hamed:** Hydrothermal method. **Yusri Md Yunos:** Funding acquisition, article editing. **Mohamed Sultan Mohamed Ali:** Funding acquisition, Conceptualization, Validation,

writing, Supervision, and, Writing – review & editing.

Declaration of competing interest

The authors declare the following financial interests/personal relationships which may be considered as potential competing interests: Mohamed Sultan Mohamed Ali reports financial support and equipment, drugs, or supplies were provided by Universiti Teknologi Malaysia School of Electrical Engineering. Mohamed Sultan Mohamed Ali reports financial support was provided by Ministry of Higher Education Malaysia.

Data availability

Data will be made available on request.

Acknowledgement

References

[1] S. Kathirvel, S. Pedaballi, C. Su, B.R. Chen, W.R. Li, Morphological control of TiO2 nanocrystals by solvothermal synthesis for dye-sensitized solar cell applications, Appl. Surf. Sci. 519 (August 2019) 2020, https://doi.org/10.1016/j.apsusc.2020.146082.

[2] J. Wang, X. Nie, W. Wang, Z. Zhao, L. Li, Z. Zhang, Single-layer graphene-TiO2 nanotubes array heterojunction as photoanode to enhance the photoelectric of DSSCs, Optik 242 (February) (2021), https://doi.org/10.1016/j.ijleo.2021.167245.

[3] A. Hidayat, et al., Synthesis and characterization of TiO2/ZnO-Ag@TiO2 nanocomposite and their performance as photoanode of organic Dye-Sensitized Solar Cell, Mater. Today Proc. 44 (2021) 3395–3399, https://doi.org/10.1016/j.matpr.2020.11.862.

[4] N. Sriharan, T.S. Senthil, P. Soundarrajan, M. Kang, Surface modification of TiO2 nanorods with Mg doping for efficient photoelectrodes in dye sensitized solar cells, Appl. Surf. Sci. 585 (January) (2022) 1–14, https://doi.org/10.1016/j.apsusc.2022.152719.

[5] A. Panepinto, A. Krumpmann, D. Cornil, J. Cornil, R. Snyders, Switching the electrical characteristics of TiO2 from n-type to p-type by ion implantation, Appl. Surf. Sci. 563 (April) (2021), https://doi.org/10.1016/j.apsusc.2021.150274.

[6] M.M.I.M. Hasnan, et al., Improvement of facile hydrothermal TiO2 rutile nanorod-flower using second HiPIMS deposition for DSSC performance enhancement, Opt. Mater. 117 (April) (2021).

[7] Y. Xu, et al., Ag-encapsulated Single-Crystalline Anatase TiO2 Nanoparticle photoanodes for enhanced dye-sensitized solar cell performance, J. Alloys Compd. 695 (2017) 1104–1111, https://doi.org/10.1016/j.jallcom.2016.10.236.

[8] V. Etacheri, C. Di Valentin, J. Schneider, D. Bahnemann, S.C. Pillai, Visible-light activation of TiO2 photocatalysts: advances in theory and experiments, J. Photochem. Photobiol. C Photochem. Rev. 25 (Dec. 2015) 1–29, https://doi.org/10.1016/j.jphotochemrev.2015.08.003.

[9] A. Bartkowiak, O. Korolevych, G.L. Chiarello, M. Makowska-Janusik, M. Zalas, Experimental and theoretical insight into dsscs mechanism influenced by different doping metal ions, SSRN Electron. J. 597 (May) (2022), https://doi.org/10.2139/ssrn.4050264.

[10] D. Kishore Kumar, et al., Functionalized metal oxide nanoparticles for efficient dye-sensitized solar cells (DSSCs): a review, Mater. Sci. Energy Technol. 3 (2020) 472–481, https://doi.org/10.1016/j.mset.2020.03.003.

[11] N.G. Park, J. Van De Lagemaat, A.J. Frank, Comparison of dye-sensitized rutile- and anatase-based TiO2 solar cells, J. Phys. Chem. B 104 (38) (2000) 8989–8994, https://doi.org/10.1021/jp994365l.

[12] M. Shakeel Ahmad, A.K. Pandey, N. Abd Rahim, Advancements in the development of TiO2 photoanodes and its fabrication methods for dye sensitized solar cell (DSSC) applications. A review, Renew. Sustain. Energy Rev. 77 (January) (2017) 89–108, https://doi.org/10.1016/j.rser.2017.03.129.

[13] N.A. Karim, U. Mehmood, H.F. Zahid, T. Asif, Nanostructured photoanode and counter electrode materials for efficient Dye-Sensitized Solar Cells (DSSCs), Sol. Energy 185 (January) (2019) 165–188, https://doi.org/10.1016/j.solener.2019.04.057.

[14] S.B. Wategaonkar, et al., Structural, morphological, and optical studies of hydrothermally synthesized Nb-added TiO2 for DSSC application, *Ceram. Int.*, no. June (2021), https://doi.org/10.1016/j.ceramint.2021.05.284.

[15] Q. Liu, J. Wang, Dye-sensitized solar cells based on surficial TiO2 modification, Sol. Energy 184 (April) (2019) 454–465, https://doi.org/10.1016/j.solener.2019.04.032.

[16] M. Muralidharan, S. Selvakumar, K. Sivakumar, K. Sivaji, Effect of Yb doping on structural, optical and induced ferromagnetism in SrSnO3 perovskite nanostructures, Phys. B Condens. Matter 615 (April) (2021), https://doi.org/10.1016/j.physb.2021.413039.

[17] F. Babar, et al., Nanostructured photoanode materials and their deposition methods for efficient and economical third generation dye-sensitized solar cells: a comprehensive review, Renew. Sustain. Energy Rev. 129 (June) (2020), 109919, https://doi.org/10.1016/j.rser.2020.109919.

[18] J. Prakash, S. Sun, H.C. Swart, R.K. Gupta, Noble metals-TiO2 nanocomposites: from fundamental mechanisms to photocatalysis, surface enhanced Raman scattering and antibacterial applications, Appl. Mater. Today 11 (2018) 82–135, https://doi.org/10.1016/j.apmt.2018.02.002.

[19] R. Jose, V. Thavasi, S. Ramakrishna, Metal oxides for dye-sensitized solar cells, J. Am. Ceram. Soc. 92 (2) (2009) 289–301, https://doi.org/10.1111/j.1551-2916.2008.02870.x.

[20] B.V. Dias, G.T. Tractz, A. Viomar, G.A.R. Maia, M.T. da Cunha, P.R.P. Rodrigues, Photoelectrochemical behavior of the cell FTO/TiO2/CeO2/N719 obtained from the pechini and precipitation of cerium oxide methods, J. Electron. Mater. 47 (9) (2018) 5556–5563, https://doi.org/10.1007/s11664-018-6465-5.

[21] H.A. Deepa, G.M. Madhu, V. Venkatesham, Performance evaluation of DSSC's fabricated employing TiO2 and TiO2-ZnO nanocomposite as the photoanodes, Mater. Today Proc. 46 (xxxx) (2021) 4579–4586, https://doi.org/10.1016/j.matpr.2020.09.711.

[22] K. Mahmood, H.W. Kang, R. Munir, H.J. Sung, A dual-functional double-layer film with indium-doped ZnO nanosheets/nanoparticles structured photoanodes for dye-sensitized solar cells, RSC Adv. 3 (47) (2013) 25136–25144, https://doi.org/10.1039/c3ra43643h.

[23] F. Khojasteh, M.R. Mersagh, H. Hashemipour, The influences of Ni, Ag-doped TiO2 and SnO2, Ag-doped SnO2/TiO2 nanocomposites on recombination reduction in dye synthesized solar cells, J. Alloys Compd. 890 (2021) 13, https://doi.org/10.1016/j.jallcom.2021.161709.

[24] Q. Wali, A. Fakharuddin, R. Jose, Tin oxide as a photoanode for dye-sensitised solar cells: current progress and future challenges, J. Power Sources 293 (2015) 1039–1052, https://doi.org/10.1016/j.jpowsour.2015.06.037.

[25] A. Roy, S. Bhandari, S. Sundaram, T.K. Mallick, Intriguing CeO2–TiO2 hybrid nanostructured photoanode resulting up to 46% efficiency enhancement for dye-sensitized solar cells, Mater. Chem. Phys. 272 (July) (2021), https://doi.org/10.1016/j.matchemphys.2021.125036.

[26] Y. Liu, H. Ran, J. Fan, X. Zhang, J. Mao, G. Shao, Fabrication and photovoltaic performance of niobium doped TiO2 hierarchical microspheres with exposed {001} facets and high specific surface area, Appl. Surf. Sci. 410 (2017) 241–248, https://doi.org/10.1016/j.apsusc.2017.03.085.

[27] K. Aravinthkumar, E. Praveen, A.J. Regina, C.R. Mohan, Investigation on SrTiO3 nanoparticles as a photocatalyst for enhanced photocatalytic activity and photovoltaic applications, December 140 (2021) 2022.

[28] F. Saadat, A. Alizadeh, M. Roudgar-amoli, Z. Shariatinia, Exploring the Influence of Zn2SnO4/ZIF-8 Nanocomposite Photoelectrodes on Boosting Efficiency of Dye Sensitized Solar Cells," No, February, 2022.

[29] N. Purushotham Reddy, R. Santhosh, J.M. Fernandes, R. Muniramaiah, B. Murali, D. Paul Joseph, Nanocrystalline Sb-doped-BaSnO3 perovskite electron transport layer for dye-sensitized solar cells, Mater. Lett. 311 (September 2021) 2022, https://doi.org/10.1016/j.matlet.2021.131629.

[30] K.P. Ong, X. Fan, A. Subedi, M.B. Sullivan, D.J. Singh, Transparent conducting properties of SrSnO3 and ZnSnO3, Apl. Mater. 3 (6) (2015), https://doi.org/10.1063/1.4919564.

[31] S. Jin, et al., Preparation and characterization of Sm3+-doped SrSnO3 and its photoelectric performance as photo-anode of dye-sensitized solar cells, J. Nanoparticle Res. 19 (8) (2017), https://doi.org/10.1007/s11051-017-3986-4.

[32] Y. Li, H. Zhang, B. Guo, M. Wei, Enhanced efficiency dye-sensitized SrSnO3 solar cells prepared using chemical bath deposition, Electrochim. Acta 70 (2012) 313–317, https://doi.org/10.1016/j.electacta.2012.03.078.

[33] H. Mohammadian-Sarcheshmeh, R. Arazi, M. Mazloum-Ardakani, Application of bifunctional photoanode materials in DSSCs: a review, Renew. Sustain. Energy Rev. 134 (August) (2020), 110249, https://doi.org/10.1016/j.rser.2020.110249.

[34] N.K.A. Hamed, et al., Dependence of photocatalysis on electron trapping in Ag-doped flowerlike rutile-phase TiO2 film by facile hydrothermal method, Appl. Surf. Sci. 534 (August) (2020), 147571, https://doi.org/10.1016/j.apsusc.2020.147571.

[35] N.D. Desai, K.V. Khot, T. Dongale, K.P. Musselman, P.N. Bhosale, Development of dye sensitized TiO2 thin films for efficient energy harvesting, J. Alloys Compd. 790 (2019) 1001–1013, https://doi.org/10.1016/j.jallcom.2019.03.246.

[36] A. Zatirostami, Increasing the efficiency of TiO2-based DSSC by means of a double layer RF-sputtered thin film blocking layer, Optik 207 (November) (2019) 2020, https://doi.org/10.1016/j.ijleo.2020.164419.

[37] H.L. Ma, J.Y. Yang, Y. Dai, Y.B. Zhang, B. Lu, G.H. Ma, Raman study of phase transformation of TiO 2 rutile single crystal irradiated by infrared femtosecond laser, Appl. Surf. Sci. 253 (18) (2007) 7497–7500, https://doi.org/10.1016/j.apsusc.2007.03.047.

[38] M.C.F. Alves, et al., Influence of synthesis conditions on carbonate entrapment in perovskite SrSnO3, Mater. Lett. 63 (1) (2009) 118–120, https://doi.org/10.1016/j.matlet.2008.09.023.

[39] T. Rajaramanan, G.R.A. Kumara, D. Velauthapillai, P. Ravirajan, M. Senthilnanthanan, Ni/N co-doped P25 TiO2 photoelectrodes for efficient Dye-Sensitized Solar Cells, Mater. Sci. Semicond. Process. 135 (April) (2021), 106062, https://doi.org/10.1016/j.mssp.2021.106062 [Online]. Available:.

[40] T. Ponken, S. Kongsankham, S. Panya, W. Choawunklang, P. Ardchongthong, Effect of titanium dioxide (TiO2) light scattering layer deposited by spray deposition method at room temperature for dye-sensitized solar cell (DSSC), Mater. Today Proc. 17 (2019) 1249–1258, https://doi.org/10.1016/j.matpr.2019.06.013.

[41] P. Gnida, et al., Impact of blocking layer on DSSC performance based on new dye -indolo[3,2,1-jk]carbazole derivative and N719, Dyes Pigments 200 (January) (2022), https://doi.org/10.1016/j.dyepig.2022.110166.

[42] T. Potlog, L. Ghimpu, V. Suman, A. Pantazi, M. Enachescu, Influence of RF sputtering power and thickness on structural and optical properties of NiO thin films, Mater. Res. Express 6 (9) (2019), https://doi.org/10.1088/2053-1591/ab317d.

[43] E. Hasani, Effect of treatment time and radio frequency power on roughness and wettability of oxygen plasma-etched Cadmium Telluride thin films, Thin Solid Films 761 (February) (2022), https://doi.org/10.1016/j.tsf.2022.139499.

[44] Y. Zhong, et al., Influence mechanism of RF bias on microstructure and superconducting properties of sputtered niobium thin films, Vacuum 207 (October 2022) 2023, https://doi.org/10.1016/j.vacuum.2022.111636.

[45] W. Zhang, X. Pei, J. Chen, H. He, Effects of Al doping on properties of xAl-3%In-TiO2 photocatalyst prepared by a sol-gel method, Mater. Sci. Semicond. Process. 38 (2015) 24–30, https://doi.org/10.1016/j.mssp.2015.04.007.

[46] Y.H. Nien, et al., Enhanced photovoltaic conversion efficiency in dye-sensitized solar cells based on photoanode consisting of TiO2/GO/Ag nanofibers, Vacuum 167 (December 2018) (2019) 47–53, https://doi.org/10.1016/j.vacuum.2019.05.022.

[47] T. Wu, X. Kang, M.W. Kadi, I. Ismail, G. Liu, H. Cheng, Enhanced photocatalytic hydrogen generation of mesoporous rutile TiO2 single crystal with wholly exposed {111} facets, Chin. J. Catal. 36 (2015) 2103–2108, https://doi.org/10.1016/S1872, 0.

[48] X. Liu, et al., Visible light active pure rutile TiO2 photoanodes with 100% exposed pyramid-shaped (111) surfaces, Nano Res. 5 (11) (2012) 762–769, https://doi.org/10.1007/s12274-012-0259-5.

[49] A.M. Al-Baradi, Sputtered and heat-treated TiO2 electrodes for dye-sensitized solar cells applications, Results Phys. 17 (March) (2020), https://doi.org/10.1016/j.rinp.2020.103109.

[50] H.S. Abdullah, I.A. Qattan, Z.M. Albataineh, A.D. Telfah, Optical, structural, and crystal defects characterizations of dip synthesized (Fe-Ni) Co-doped ZnO thin films, Mater. (Basel, Switzerland) 13 (7) (2020) 17, https://doi.org/10.3390/ma13071737, 173.

[51] Y.X. Dong, X.L. Wang, E.M. Jin, S.M. Jeong, B. Jin, S.H. Lee, One-step hydrothermal synthesis of Ag decorated TiO2 nanoparticles for dye-sensitized solar cell application, Renew. Energy 135 (2019) 1207–1212, https://doi.org/10.1016/j.renene.2018.12.062.